Analysis of the mechanical anisotropy of stereolithographic 3D printed polymer composites

Johannes Stögerer, Sonja Baumgartner, Thaddäa Rath & Jürgen Stampfl

Published online: 26 Feb 2022.

Submit your article to this journal ⬈

View related articles ⬈

View Crossmark data ⬈

Citing articles: 1 View citing articles ⬈

Routledge
Taylor & Francis Group

∂ OPEN ACCESS | Check for updates

Analysis of the mechanical anisotropy of stereolithographic 3D printed polymer composites

Johannes Stögerer, Sonja Baumgartner, Thaddäa Rath and Jürgen Stampfl

Institute of Materials Science and Technology, TU Wien, Vienna, Austria

ABSTRACT

3D printing is a manufacturing technique based on the structuring of parts layer by layer. This principle yields a specific printing direction, that is the spatial orientation of the produced layers. Thus, potential anisotropy arising from the printing direction is a major concern in 3D printing. The mechanical properties of a biocompatible resin mainly consisting of methacrylates and tricalcium phosphate particles is examined. Various tests are conducted to examine the mechanical anisotropy of testing samples manufactured with a 3D printer based on stereolithography. A digital light processing unit ($\lambda = 375\,nm$) is utilized to produce test samples in three orthogonal directions. Bending behaviour, fracture toughness, and hardness are measured. Furthermore, light microscopy is utilized to assess the properties of the fractured samples qualitatively. Assessed values are in agreement with comparable materials and show no statistically significant ($p = 0.095$) evidence of anisotropic behaviour. Sample orientation has no impact on the mechanical properties of the produced parts. Thus, production time and capabilities can be optimized by varying and combining sample orientation without changing the mechanical performance of the engineered parts significantly.

CONTACT Johannes Stögerer ✉ johannes.stoegerer@tuwien.ac.at ▢ Institute of Materials Science and Technology, TU Wien, Vienna, Austria.

1. Introduction

Additive manufacturing (AM), also known as 3D printing is a manufacturing procedure based on the structuring of parts layer by layer (Aliheidari, Tripuraneni, Ameli, & Nadimpalli, 2017). Ever since the first invention of this method in 1986, this technology has been evolved and diversified (Bandyopadhyay & Heer, 2018; Domingo-Espin et al., 2015; Quenard, Dorival, Guy, Votie, & Brethome, 2018; Wang, Jiang, Zhou, Gou, & Hui, 2017). Stereolithography (SLA) is the oldest and one of the most commonly used concepts in polymer 3D printing (Bekas, Hou, Liu, & Panesar, 2019; Ngo, Kashani, Imbalzano, Nguyen, & Hui, 2018; Wang, Zhou, Lin, Corker, & Fan, 2020). It offers exceptional spatial resolution and surface quality (Rath et al., 2021). This technology is based on the solidification of liquid monomers in a vat via polymerization, induced by light either in the visible or ultraviolet (UV) spectrum (Ngo et al., 2018; Wang et al., 2020). Liquid resins are mostly based on (meth-) acrylates, which are cured by free radical photopolymerization. Exposure to an appropriate light source triggers the creation of free radicals and the polymerization of the (meth-)acrylates (Wang et al., 2017). Additional components can be added to adapt the properties of the final building printed part. These additives include, among others, absorbers to prevent light scattering, coloring agents, additives to prevent sedimentation and increase shelf live, or fillers (Ligon, Liska, Stampfl, Gurr, & Mülhaupt, 2017).

3D printing methods are suitable for the production of individually customized shapes and very fine and delicate structures. However, the fundamental principle of layer-wise structuring yields a specific printing direction (i.e., spatial orientation of the printed layers). Studies on AM technologies have shown that the building direction can result in an anisotropic behavior (Casavola, Cazzato, Moramarco, & Pappalettere, 2016; Kim et al., 2020; McLouth, Severino, Adams, Patel, & Zaldivar, 2017; Monzon, Ortega, Hernandez, Paz, & Ortega, 2017; Shanmugasundaram, Razmi, Mian, & Ladani, 2020). In contrast, other studies found nearly isotropic behavior of parts build with AM technologies (Hague, Mansour, Saleh, & Harris, 2004; Kazmer & Kutz, 2017; Li et al., 2020). Consistently, research has found contrasting results for the SLA process with respect to potential anisotropy (Chantarapanich, Puttawibul, Sitthiseripratip, Sucharitpwatskul, & Chantaweroad, 2013; Cosmi & Dal Maso, 2020; Dizon, Espera, Chen, & Advincula, 2018; Dulieu-Barton & Fulton, 2000). Simulation studies confirm the complex material behavior, depending on various factors (Guessasma et al., 2018; Li et al., 2015; Manière, Harnois, & Marinel, 2021; Markandan, Seetoh, & Lai, 2021; Wu, Xu, Zhang, & Guo, 2020). Thus, potential anisotropic behavior is an important property, which has to be considered in AM processes (Lai et al., 2021).

In SLA, the dimensions of the building platform limit the building space. To maximize part production, it is imperative to utilize the available space as efficiently as possible. Thus, potential anisotropy limiting the sample orientation might influence the building time as well as the production capability. This might imply various building directions of samples in the same printing job. Moreover, different building directions are related to diverse amounts of total layers required resulting in greatly varying building times. Therefore, knowledge about anisotropic behavior is crucial for the strategic planning of production cycles.

In this study, liquid resins based on various methacrylates and tricalcium phosphate (TCP) as particulate filler are utilized to create a ceramic composite by means of 3D printing. Methacrylates offer favorable properties including optical transparency, mechanical stability, good curing, and surface quality, as well as outstanding spatial resolution (Ligon et al., 2017). Finished products are stiff and strong, granting good load bearing (Gorsche et al., 2016). Strength and stiffness are further increased by the addition of TCP powder. However, parts based on methacrylates are susceptible to crack growth resulting in low fracture toughness and brittle material behavior (Ligon-Auer, Schwentenwein, Gorsche, Stampfl, & Liska, 2015). In this printing unit, a digital light processing (DLP) mask cures the desired shape instead of a single laser point used in conventional SLA. DLP is based on an array of small mirrors combined in a digital micro-mirror device (DMD). The position of these mirrors can be altered between two states by micro-actuators (Kundu et al., 2020). Depending on mirror orientation, exposed light rays are reflected or transmitted to the surface of the material vat. The latter resulting in curing of the location correspondent to a specific pixel of the DMD. Thus, spatial resolution is essentially dependent on the number of mirrors in the DMD as well as the optical characteristics. The device present provides Full HD resolution with a pixel size of 50 μm. Since all pixels of the desired shape can be cured simultaneously, DLP technology greatly reduces printing time in comparison to conventional SLA (Zhiquan, Chong, Wanwan, & Ren, 2019).

The selection of raw materials for the present resin is influenced by already existing industrial applications. TCP possesses excellent biocompatibility (i.e., ability of a material to trigger an appropriate host response in a living organism) (Seitz, Deisinger, Leukers, Detsch, & Ziegler, 2009; Zhao et al., 2020; Zhou et al., 2020). It is a material naturally occurring in the human body (e.g., skeleton and teeth) (Williams, 2008). Therefore, it is an essential part in artificial implants granting osteoconductivity and osteoinductivity (Homaeigohar, Shokrgozar, Khavandi, & Javadpour, 2005; Vamze, Pilmane, & Skagers, 2015). In dental fillings and dental implants manufactured by 3D printing methods, resin materials based on methacrylates and filled with TCP are commonly used (Wang, Habib, & Zhu, 2018).

The aim of this study is to investigate the impact of printing directions on the properties of a 3D printed composite. A lithography-based AM system is utilized to structure test specimens in orthogonal spatial directions. Various important mechanical parameters are tested and assessed. Afterwards a more detailed evaluation via statistical methods is performed.

2. Materials and methods

2.1. Material composition

The polymerizable resin consists of liquid and solid constituents and is based on different methacrylates and a photoinitiator. This combination allows solidification via UV light and ensures sufficiently low viscosity for the printing process. Moreover, a stable dispersion of solid particles is ensured by the addition of a rheology additive and dispersing agents. Furthermore, an UV light absorber to prevent over-polymerization (i.e., solidification at non-desirable locations due to light scattering). The solid phase of the resin consists of two different components. First, fumed silica hindering particle sinking and, therefore, granting long time stability. Second, TCP particles as a filler for the manufacturing of the composite. The composition is optimized to ensure sufficiently low viscosity, long time stability, and reactivity necessary for the printing process at room temperature. The particle size distribution of the TCP powder is measured with a laser diffraction device (Mastersizer 2000, Malvern Panalytical, Malvern, UK). The resin batch viscosity is analyzed with an oscillating rheometer (MCR 102, Anton Paar, Graz, Austria). The resin composition as well as volume percentages are displayed in Table 1.

Table 1. Composition of the photocurable resin.

Component	Content
Ethoxylated 3-Bisphenol A Di-Methacrylate	33.3 wt.%
(Arkema, Colombes, France)	51.6 vol.%
-Di-functional methacrylate	5.0 wt.%
(Arkema, Colombes, France)	7.9 vol.%
Di-functional methacrylate	5.0 wt.%
(Arkema, Colombes, France)	7.7 vol.%
Polymeric dispersant – D540	1.0 wt.%
(Lubrizol, Wickliffe, USA)	1.5 vol.%
(2,4,6-trimethylbenzoyl)-	0.1 wt.%
phenylethoxyphosphine oxide (TPO-L)	
(Lambson, Wetherby, UK)	0.2 vol.%
2,2-Dihydroxy-4,4-imethoxybenzophenone	0.03 wt.%
(TCI, Tokio, Japan)	0.05 vol.%
Fumed silica (rheology additive)	0.6 wt.%
(Merck, Darmstadt, Germany)	0.9 vol.%
TCP	55.0 wt.%
(Merck, Darmstadt, Germany)	30.4 vol.%

2.2. Batch preparation

The preparation of the resin is done in a two-step procedure. In the first step, all organic substances (i.e., methacrylates, dispersing agents, and photoinitiator) are filled into a container and mixed for 10 min at a speed of 2100 rotations per minute (rpm) using a Speed Mixer™ (DAC 600.2 Vac-P, Hauschild and Co KG, Hamm, Germany). This device is connected to an external vacuum pump (MPC 301Z, Ilmvac, Illmenau, Germany). Thus, simultaneous mixing and degassing at a pressure of 5×10^{-6} bar is possible. After a homogenous batch of all organic components is achieved, the remaining inorganic particles are added to the container. The resin is mixed for another 10 min at a speed of 2100 rpm and an applied pressure of 5×10^{-6} bar to create the resin masterbatch. Long-term stability and homogeneity of the batch was observed qualitatively by filling small amounts of the resin in thin transparent test tubes. Potential component separation and sedimentation is thus better visible. Although the batch contains two components providing homogeneous particle distribution and long-term stability (i.e., dispersing agent and rheology additive), the batch is mixed and degassed prior to each printing job for 10 min at a speed of 2100 rpm and a pressure of 5×10^{-6} bar to ensure optimal particle dispersion.

2.3. 3D printing

All samples are printed using an SLA 3D printer constructed at TU Wien (Felzmann et al., 2012). The device uses UV light (Luxbeam 4600, Visitech Engineering GmbH, Wetzlar, Germany) with a wavelength of $\lambda = 375$ nm and the principle of DLP to solidify the resin at desired locations in a layer-wise process. CAD models in the standard triangulation language (STL) format are utilized. These files are converted into PNG-file format and contain the necessary information for the light exposure of each individual voxel. Theoretical minimal layer thickness achievable with this 3D printer is at about 10 μm. However, TCP powder particle size limits reproducible results to a minimal layer thickness of 25 μm. The light source provides a spatial resolution of 50 μm in horizontal axes.

The liquid resin is contained in a transparent and rotatable material vat. The building platform is immersed into the resin bath and UV light is projected through the transparent vat to cure the resin solely at desired locations. After the solidification, the building platform with the adhering layer is lifted and the vat surface is coated with fresh resin via a coating knife and vat rotation. This mechanism allows the processing of highly filled resins. Moreover, a sufficiently thin coating of about 30 μm is ensured. This thin film is essential for the structuring process of the

material layers. After the coating, the building platform is lowered into the liquid resin and the next material layer is cured. By the repetition of this process, all samples are manufactured. The penetration depth of the UV light for the filled resin is 150 µm at 35 mW/cm², thus multiple times the layer thickness, to ensure sufficient curing and bonding of the previous layers. The penetration depth is measured by curing a circular formed shape ($r = 5$ cm) in the middle of the vat. Abundant liquid resin is filled into the respective area of the vat. After the curing process, the remaining liquid material on top of the cured disc is removed and the solidified part is detached from the vat. Thereafter, the thickness of the disc, representing the penetration depth of the UV light, is measured using a digital caliper.

The first five layers of each sample are cured for 5 s while all following ones are cured for 2 s. This method provides adequate sample adherence on the building platform. The 3D printing process is displayed in Figure 1.

2.4. Sample preparation

Multiple testing samples are manufactured to analyse potential (thermo-) mechanical anisotropy of the composite material present. All specimens are manufactured in XYZ, YZX, and ZXY direction according to DIN EN ISO/ASTM 52921 with the same 3D printer. Thus, three groups of samples with orthogonal layer directions are built. A schematic view of samples in XYZ, YZX, and ZXY direction adhering to a building platform is depicted in Figure 2.

Ambience and resin temperature are held constant at 23 °C during all printing processes. After the manufacturing, remaining resin residues on the surface of the samples are removed manually using paper tissues. In
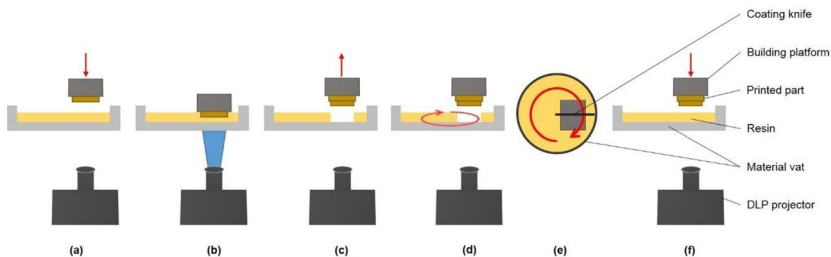

Figure 1. Workflow of the 3D-printing process. Building platform with the attached layers is immersed into the vat (a). A layer is cured by UV light and attaches to the already existing layers (b). The platform is lifted (c). Vat surface is coated with fresh resin through rotation of the vat and a stationary coating knife (d). Top view of the coating procedure (e). The process is repeated by re-immersing the platform into the resin (f).
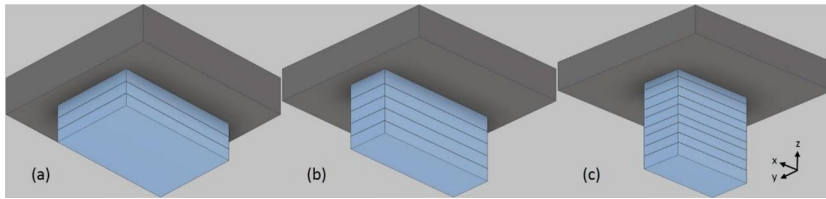
Figure 2. Schematic illustration of building platforms with layered parts in XYZ (a), YZX (b), and ZXY (c) manufacturing directions.

a last step all samples are post cured in a UV floodlight device (Intelliray 600, Uvitron, West Springfield, USA) for 10 min.

For fracture mechanical analysis, 3-point bending test specimens with a width of 50 mm are manufactured according to ISO 13586. After the building process, in agreement with ISO 13586, a notch is created using a notching device (Notchvis 6951, Ceast, Pianezza. Italy) as well as a sharp razor blade.

Bending test specimens according to DIN EN ISO 178 are printed. In agreement with DIN EN ISO 178, standard dimensions for these specimens are adapted to 50 mm × 10 mm × 3.2 mm for length, width, and height, respectively. Space on the building platform is limited, thus preventing the construction of standard bending test parts. After the construction, the samples are sanded to remove superficial impurities and grant a smooth surface.

Dynstat specimens according to DIN 53435 are printed to measure fracture toughness under impact loading. Small specimen dimensions prevent notching of theses samples after the manufacturing. Thus, unnotched impact strength samples are tested. The construction of more commonly used impact testing specimens (e.g., Charpy DIN EN ISO 179-1) is not feasible due to limited building platform space.

Vickers hardness is measured according to DIN EN ISO 6507-1. Rectangular base specimens (25 mm × 10 mm × 5 mm) are printed for this test. After manufacturing, samples are sanded and polished using an automated sanding device (TegraPol-31, Struers, Willich, Germany) to ensure plane, smooth, and clean surfaces. Although DIN EN ISO 6507-1 is primarily eligible for metals, this method is commonly utilized for hardness measurements of polymers (Low, 1998; Low & Shi, 1998).

Thermo-mechanical properties are measured using dynamic mechanical analysis (DMA) according to DIN EN ISO 6721-1 in a 3-point bending set-up according to DIN EN ISO 178. Sample dimensions for this testing procedure are 25 mm × 4 mm × 2 mm in length, width, and height, respectively. After all preparation steps the samples are stored in a desiccator according to ISO 291.

2.5. Testing method

All mechanical tests are conducted at constant standard testing conditions (i.e., room temperature and humidity). Notched 3-point bending test specimens are tested using a universal testing machine type Zwick Z050 (ZwickRoell, Ulm, Germany) until fracture. Individual displacement corrections for each printing direction are conducted with additional specimens according to ISO 13586. These measurements allow to assess the critical stress intensity factor K_{Ic}. This parameter quantifies the specific amount of local stress at a crack tip, which induces uncontrolled crack growth and thus specimen failure. It is calculated via the formula

$$K_{IC} = f\left(\frac{a}{w}\right) \star \frac{F_Q}{h^\star \sqrt{w}} \tag{1}$$

where $f(a/w)$ is a geometry factor, h, and w are specimen thickness and width, respectively, and F_Q is the load at crack growth initiation. The index "I" denotes mode I loading, in which the applied loading is perpendicular to the plane of the crack. Mode I loading is considered the most severe and most important one (Sherry & Marrow, 2010). The setup used offers a minimal span width of 40 mm, which is sufficient for the dimension of the tested specimens. Data analysis is conducted via the corresponding software testXpertIII (Version 3.6, ZwickRoell, Ulm, Germany). A deformation rate of 10 mm/min and a preloading of 0.15 MPa are used as testing preconditions for all bending tests. 10 samples of each group are tested.

The investigation of bending properties is conducted using the same testing machine type Zwick Z050 (ZwickRoell, Ulm, Germany) and analytical software testXpertIII (Version 3.6, ZwickRoell, Ulm, Germany). Preloading of 0.1 MPa and deformation rate of 1 mm/min are defined for all bending tests. 10 samples of each group are tested with this set-up.

Dynstat specimens are tested using a pendulum impact tester Frank 573 (Karl Frank GmbH, Weinheim, Germany) with a 1 J hammer attached. Samples are fixed between two thrust blocks and punched by the hammer attached to the pendulum. Complete fracture of the samples is necessary to yield valid results. The difference in height reached by the hammer is equal to the energy absorbed by the specimen. The fracture toughness a_{dU} of the specimen is calculated via the formula

$$a_{dU} = \frac{E_c}{h^\star b} \tag{2}$$

where E_c is the absorbed energy, h is the specimen thickness, and b is the specimen width. 12 samples of each group are tested.

All hardness tests are performed using a HV1 set-up (M1C 010, EmcoTest, Kuchl, Austria). These parameters result in well-defined indentations marks, which are essential for the optical identification and measurement of the diagonal length. A light microscopy is integrated in the hardness testing device and a 178-magnification lens is utilized to analyze indentation marks. Eight different indentation marks distributed on the specimen surface are measured on each sample to gain higher valid results. Figure 3 shows a schematic view of the indentation positions.

Hardness values are computed automatically by virtue of indentation diagonal length. The final hardness value for each specimen is the mean of these eight measurements. 10 samples of each group are tested.

For DMA measurements, a dynamic mechanical analysis testing device D850 (TA Instruments, New Castle, USA) and the testing software Trios (TA Instruments, New Castle, USA) are utilized. All DMA measurements are conducted in a temperature range from −50 °C to 110 °C. In a first step, the sample is cooled to –50 °C using liquid nitrogen. Thereafter, the chamber temperature is held constant at −50 °C for 5 min to ensure homogeneous temperature distribution in all sample regions. Finally, the sample is heated up to 110 °C with a chosen heating rate of 3 °C per minute. All samples are preloaded with 0.1 N and examined at a constant frequency and amplitude of 1 Hz and 20 µm, respectively. One sample of each group is tested in accordance with DIN EN ISO 6721-1.
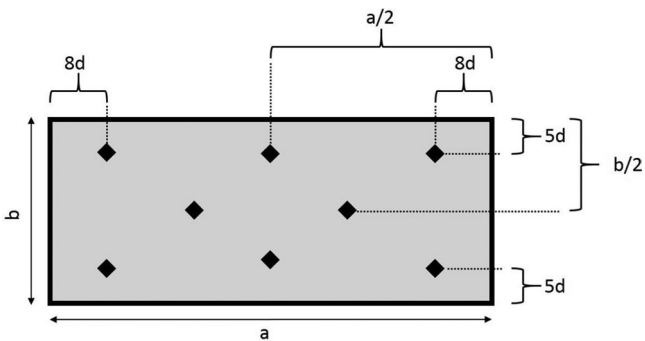

Figure 3. Positioning of Vickers indentation marks fixed by diagonal length of indentations and distance to the specimen boundaries. The distance between two adjacent marks is bigger than 10*d.

2.6. Statistical analysis

Statistical analysis is performed using SPSS® Statistics (Version 27, IBM, Armonk, USA). In order to test differences between three independent groups (i.e., printing directions XYZ, YZX, and ZXY) the ANOVA method is performed. This method compares means in dependent factors (e.g., hardness) of independent groups to find significant differences within these factors. Level of significance is determined at $p = 0.05$. ANOVA requires normal distribution of all dependent variables as well as homogeneity of variances in these factors (Cribbie, Fiksenbaum, Keselman, & Wilcox, 2012). Normal distribution of all dependent factors is tested via the Shapiro–Wilk test due to its high test power rendering it more suitable for small samples than the Kolmogorov–Smirnoff test (Razali & Wah, 2011). Homogeneity of variance is tested using the Levene test with a determined significance level of $p = 0.05$.

In case the requirements of the ANOVA are not met, the Welch-ANOVA represents a more robust alternative method to the ANOVA (Lantz, 2013). While the ANOVA based on the F statistics is very sensitive to non-normality, the Welch-ANOVA, which uses weights reduces the effect of non-normality and heteroscedasticity (Celik & Welch's, 2020). Thus, the Welch-ANOVA is a preferable method to the ANOVA in the aforementioned circumstances (Blanca, Alarcon, Arnau, Bono, & Bendayan, 2017; Jan & Shieh, 2014; Levy, 1978).

3. Results

The mean TCP particle size is 8.769 µm (d_{50}) with particle sizes ranging from 2.000 µm to 20.000 µm. The batch viscosity is 10 Pa·s at 23 °C and showed ample long-term stability throughout the duration of the study.

Statistical methods are used to reveal potential significant differences in mechanical behavior of all printing directions present. In a first step, the Shapiro–Wilk test is performed to test all dependent factors for normal distribution. In the next calculation step, the homogeneity of variances is tested for all factors using the Levene test. Results of these two tests are displayed in Table 2.

Table 2. Results of Shapiro–Wilk test and Levene test; *significant difference ($p = 0.05$).

Dependent factor	Normal distribution (Shapiro–Wilk test)	Homogeneity of variances (Levene test)
Bending modulus	0.589	0.332
Bending strength	0.236	0.286
Elongation at break	0.027*	0.561
K_{Ic}	0.508	0.720
HV1	0.455	0.152

The test confirms normal distribution for all dependent variables except elongation at break. The Shapiro–Wilk test yields a statistically significant result ($p = 0.027$) for the variable elongation at break. The Levene test confirms homogeneity of variances for all parameters. Thus, the ANOVA can be performed to analyze all parameters except elongation at break. In order to examine this parameter, the Welch-ANOVA, is conducted.

3.1. Fracture mechanical analysis

Samples are preloaded with the notch facing upwards. Specimen displacement as a function of applied force is recorded. First, material behavior is analysed qualitatively. Second, fracture toughness is calculated for each specimen. Figure 4 shows one representative curve from each respective group.

All specimens show almost ideal linear elastic behavior (i.e., linear correlation between force and displacement until point of fracture). Therefore, fracture toughness can be determined by calculation of the critical stress intensity factor K_{Ic}. Calculations according to ISO 13586 yield $1.62\,MPa{\ast}m^{(1/2)} \pm 0.14\,MPa{\ast}m^{(1/2)}$, $1.67\,MPa{\ast}m^{(1/2)} \pm 0.13\,MPa{\ast}m^{(1/2)}$, and $1.52\,MPa{\ast}m^{(1/2)} \pm 0.05\,MPa{\ast}m^{(1/2)}$ for XYZ, YZX, and ZXY, respectively. Means and standard deviations are displayed in Figure 5.
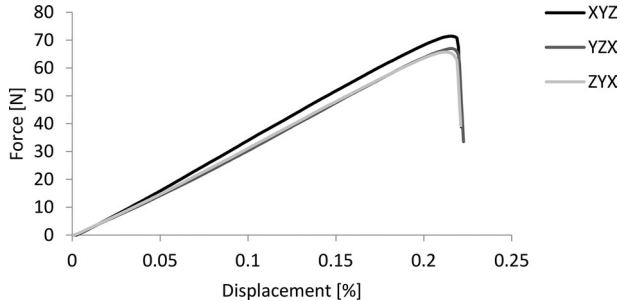

Figure 4. Representative curve of 3-point bending test specimens for each respective group shows clear linear elastic behavior.
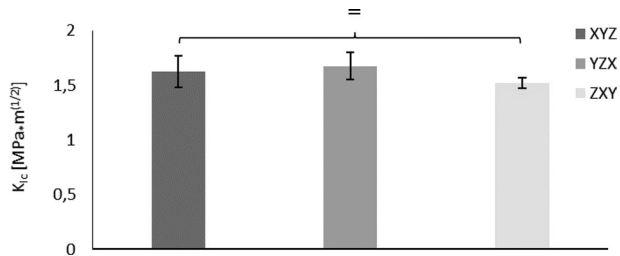

Figure 5. Influence of building directions on fracture toughness K_{Ic}. Marks (=) ANOVA shows no significant differences between either group.

Qualitative analysis of the fracture surfaces is done using a digital light microscope VHX-6000 (Keyence, Osaka, Japan). Fracture surfaces of samples from all three groups are depicted in Figure 6.

Fracture surfaces of samples from all three groups show similar features. Smooth and plain surfaces indicate abrupt specimen failure, that is no plastic deformation by the samples.

3.2. Behavior under bending conditions

Bending tests are performed to measure various material parameters. Bending modulus, bending strength, and elongation at break are measured and compared. Results of these parameters are summarized in Table 3 and displayed in Figure 7, respectively.

3.3. Toughness under impact loading

Unnotched Dynstat impact specimens are placed firmly between the thrust blocks and tested within one hour. Measured impact strength values are $6.51 \, kJ/m^2 \pm 1.27 \, kJ/m^2$, $7.30 \, kJ/m^2 \pm 1.76 \, kJ/m^2$, and $5.76 \, kJ/m^2 \pm 0.84 \, kJ/m^2$ for groups XYZ, YZX, and ZXY, respectively. Results are displayed graphically in Figure 8.
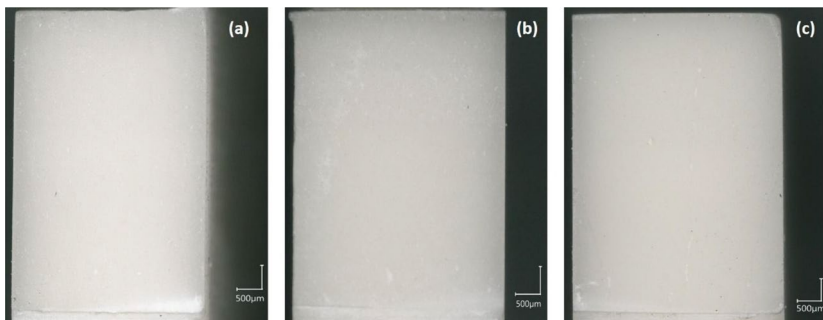

Figure 6. Fracture surface of 3-point bending specimens in XYZ (a), YZX (b), and ZXY (c) direction. Artificially introduced crack is visible as an edge on the bottom.

Table 3. Results of the bending tests.

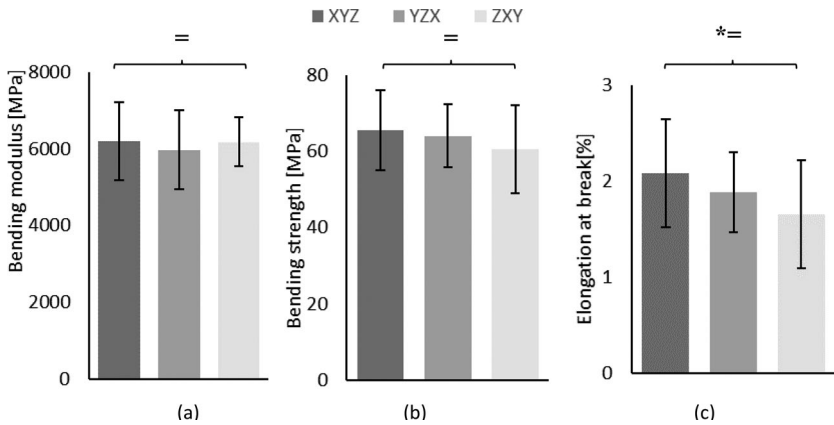| Parameter	XYZ	YZX	ZXY
Bending modulus [MPa]	6200 ± 1020	5962 ± 1032	6175 ± 644
Bending strength [MPa]	65.4 ± 10.5	64.0 ± 8.2	60.5 ± 11.7
Elongation at break [%]	2.09 ± 0.56	1.89 ± 0.41	1.65 ± 0.56

Figure 7. Influence of building direction on bending modulus (a), bending strength (b), and elongation at break (c). Marks (=) no significant differences between either group (ANOVA).

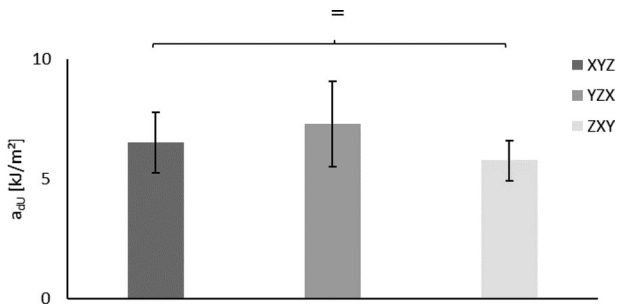*Calculation is performed with the Welch test.

Figure 8. Influence of building directions on the impact strength. Marks (=) ANOVA shows no significant differences between either group.

3.4. Hardness analysis

Sanded and polished specimens are tested within 2 h. Each hardness value represents a mean of eight indentation measurements on different locations of the sample surface. Mean HV 1 values are 27.5 ± 0.9 for XYZ, 27.0 ± 0.5 for YZX, and 26.4 ± 0.6 for ZXY. The results are displayed in Figure 9.

3.5. Dynamic mechanical analysis

Results of the DMA measurements of samples from the three building directions are displayed in Figure 10.
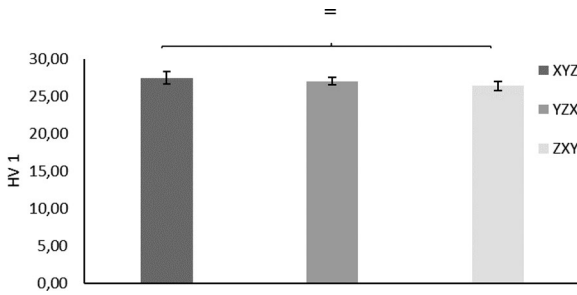
Figure 9. Influence of building directions on Vickers hardness. Marks (=) ANOVA shows no significant differences between either group.
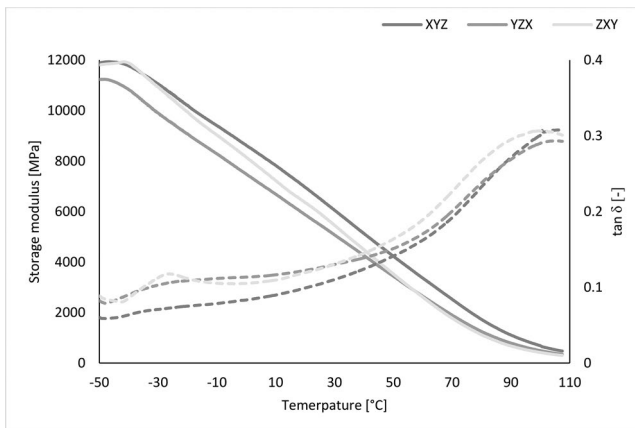

Figure 10. Results of the DMA measurements. Storage moduli (continuous line) and tan δ (dashed line) for sample orientation XYZ, YZX, and ZXY.

4. Discussion

The main aim of this study is to analyze potential mechanical anisotropy of a 3D printed ceramic composite. This composite is structured via usage of base materials commonly used in industrial applications. The printer used in this study allows the processing of highly filled polymer resins to produce structures featuring delicate details and high surface quality. A printed part for demonstration purposes is depicted in Figure 11.

Various (thermo-) mechanical tests are conducted to give a broad overview on material behavior with regard to the building direction. This is very important since layer-wise build-up of specimens is fundamental for the stereolithographic manufacturing process. Thus, structural anisotropy arises from the manufacturing process itself. Different numbers of layers necessary to complete the 3D printing job characterize the various building directions. Each layer implies the possibility for small impurities
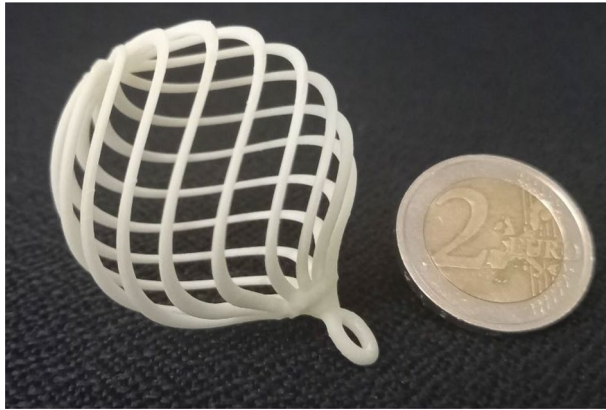
Figure 11. Possible printing resolution illustrated by a detailed structured part.

within. Additionally, each interface between two layers represents a potential weak point due to imperfect adherence and curing. The ceramic fillers utilized in this study represent a source of anisotropy. Their size as well as their shape vary to a certain amount. Hence, the exact amount of filler as well as their orientation in each layer might differ. In the present study, however, (thermo-) mechanical measurements and statistical analysis reveal no evidence for significant anisotropic behavior under the conducted testing procedures. These findings imply that manufacturing processes with this composition can be optimized in terms of efficiency. Although curing time of DLP systems is reduced compared to SLA this method remains time consuming and is greatly dependent on the building direction of the desired parts (e.g., manufacturing time of bending test specimens is 2 h for XYZ direction and over 20 h for ZXY direction). Furthermore, building parts can be orientated in varying directions to optimize usage of the limited building platform space.

Results of fracture mechanic tests with single edged specimens reveal almost ideal linear elastic fracture behavior to the point of fracture. This material behavior is expected because of high filler content and methacrylate usage. Therefore, it is reasonable to use a linear elastic fracture mechanics approach to calculate fracture toughness of the specimens present. The obtained values are in agreement with other fracture toughness measurements from similar resins (Beigi, Yeganeh, & Atai, 2013; Chai, Wang, & Sun, 2019).

For hardness measurements, a Vickers indenter is used. Although this procedure is most commonly used for the analysis of metals and is not normed for polymers it is of particular importance for instrumented hardness measurements (Grellmann & Seidler, 2015). This method allows continuous measurement of penetration depth and applied force during

the entire test. To ensure comparability of the results with future studies where instrumented hardness measurements will be applied, Vickers indentation is used in the present research.

Fracture toughness is measured by virtue of two different methods, that is 3-point bending tests with single edged specimens and Dynstat specimens. Nevertheless, results obtained by these two procedures cannot be compared. While 3-point bending tests are quasi-static, Dynstat method measures toughness at impact loading. Moreover, bending tests have been edged (i.e., a crack has been introduced artificially) in comparison to Dynstat samples consisting of pristine material.

Even though ANOVA and Welch test show no significant differences in any factor for any building directions results still vary to a certain amount. Values for Vickers hardness tests and fracture mechanics tests are quite similar for all three groups with rather small standard deviations. On the contrary, results of bending tests and Dynstat impact tests vary to a bigger extend. Small specimen size due to limited building platform space increases the impact of inevitable impurities in the specimens.

Minor cracks are especially important for fracture toughness measurements at impact loading. These voids are the source of larger cracks spreading through the part eventually leading to fracture and specimen failure. Thus, results for Dynstat specimens are scattering to a bigger amount.

Mechanical properties assessed in 3-point bending tests show reasonable results, which are in agreement with other results of similar composite materials (Randolph, Palin, Leloup, & Leprince, 2016; Wille, Hölken, Galina, Adelung, & Kern, 2016). Moreover, 3-point bending tests reveal only minor elongation at break. These results concord with the linear elastic behavior examined in the fracture mechanic tests.

DMA measurements yield similar shaped curves with related characteristics for both the storage modulus and tan δ for all three examined groups. This implies similar thermo-mechanical behavior independent of layer orientation. The storage modulus connected to the elastic parameters at room temperature (i.e., 25 °C) is 6316, 5783, and 5937 MPa for XYZ, YZX, and ZXY, respectively. This is in good agreement with the results of the bending tests conducted at room temperature. The maximum values for tan δ representing the glass transition temperature are quite similar for all three building directions at 105 °C. Hence, the thermo-mechanical area of application for this composite material is quite large.

5. Conclusion

In this study, 3D printing based on the principle of DLP is used to print (thermo-) mechanical testing specimens. A ceramic composite material

is processed to manufacture test samples in three different orthogonal directions. Various (thermo-) mechanical measurements (i.e., toughness, bending behavior, hardness, and thermo-mechanical behavior) for all three groups show similar results for samples of all three building directions. Although small deviations between the building directions are found to some extent, statistical examination reveals no significant differences. Thus, in SLA 3D printing of the present photopolymer composite the building direction only has minimal influence on the material properties. Consequently, production optimization by maximizing the building platform space used and minimizing the printing time by part rotation is not impeded by anisotropic behavior.

Acknowledgments

Disclosure statement

The authors confirm that there are no relevant financial or non-financial competing interests to report.

Funding

References

Aliheidari, N., Tripuraneni, R., Ameli, A., & Nadimpalli, S. (2017). Fracture resistance measurement of fused deposition modeling 3D printed polymers. *Polymer Testing*, *60*, 94–101. http://doi.org/10.1016/j.polymertesting.2017.03.016.

Bandyopadhyay, A., & Heer, B. (2018). Additive manufacturing of multi-material structures. *Materials Science & Engineering: Part R: Reports*, *129*, 1–16. https://doi.org/10.1016/j.mser.2018.04.001.

Beigi, S., Yeganeh, H., & Atai, M. (2013). Evaluation of fracture toughness and mechanical properties of ternary thiol-ene-methacrylate systems as resin matrix for dental restorative composites. *Dental Materials*, *29*, 777–787. http://doi.org/10.1016/j.dental.2013.04.015.

Bekas, D. G., Hou, Y., Liu, Y., & Panesar, A. (2019). 3D printing to enable multifunctionality in polymer-based composites: A review. *Composites: Part B*, *179*, 1–13.

Blanca, M., Alarcon, R., Arnau, J., Bono, J., & Bendayan, R. (2017). Non-normal data: Is ANOVA still a valid option. *Psicothema*, *29*, 552–557. https://doi.org/10.7334/psicothema2016.383.

Casavola, C., Cazzato, A., Moramarco, V., & Pappalettere, C. (2016). Orthotropic mechanical properties of fused deposition modelling parts described by classical laminate theory. *Materials & Design*, *90*, 453–458. http://doi.org/10.1016/j. matdes.2015.11.009.

Celik, N., & Welch's, A. (2020). Heteroskedastic skew-t error terms. *Communications in Statistics – Theory & Methods*, *49*, 1–12. https://doi.org/10.1080/03610926.2 020.1788084.

Chai, H., Wang, X., & Sun, J. (2019). Miniature specimens for fracture toughnessevaluation of dental resin composites. *Dental Materials*, *35*, 283–291 https:// doi.org/10.1016/j.dental.2018.11.023.

Chantarapanich, N., Puttawibul, P., Sitthiseripratip, K., Sucharitpwatskul, S., & Chantaweroad, S. (2013). Study of the mechanical properties of photo-cured epoxy resin fabricated by stereolithography process. *Songklanakarin Journal of Science & Technology*, *35*, 91–98.

Cosmi, F., & Dal Maso, A. (2020). A mechanical characterization of SLA 3D-printed specimens for low-budget applications. *Materials Today: Proceedings*, *32*, 194–201 https://doi.org/10.1016/j.matpr.2020.04.602.

Cribbie, R. A., Fiksenbaum, L., Keselman, H. J., & Wilcox, R. R. (2012). Effect of non-normality on test statistics for one-way independent groups designs. *British Journal of Mathematical & Statistical Psychology*, *65*, 56–73 https://doi. org/10.1111/j.2044-8317.2011.02014.x.

Dizon, J. R. C., Espera, A. H., Chen, Q., & Advincula, R. C. (2018). Mechanical characterization of 3D-printed polymers. *Additive Manufacturing*, *20*, 44–67 https://doi.org/10.1016/j.addma.2017.12.002.

Domingo-Espin, M., Puigoriol-Forcada, J., Garcia-Granada, A.-A., Lluma, J., Borros, S., & Reyes, G. (2015). Mechanical property characterization and simulation of fused deposition modeling polycarbonate parts. *Materials & Design*, *83*, 670–677. http://doi.org/10.1016/j.matdes.2015.06.074.

Dulieu-Barton, J. M., & Fulton, M. C. (2000). Mechanical properties of a typical stereolithography resin. *Strain*, *36*(2), 81–87 https://doi. org/10.1111/j.1475-1305.2000.tb01177.x.

Felzmann, R., Gruber, S., Mitteramskogler, G., Tesavibul, P., Boccaccini, A. R., Liska, R., & Stampfl, J. (2012). Lithography-based additive manufacturing of cellular ceramic structures. *Advanced Engineering Materials*, *14*(12), 1052–1058. https://doi.org/10.1002/adem.201200010.

Gorsche, C., Seidler, K., Knaack, P., Dorfinger, P., Koch, T., Stampfl, J., … Liska, R. (2016). Rapid formation of regulated methacrylate networks yielding tough materials for lithographybased 3D printing. *Polymer Chemistry*, *7*(11), 2009–2014. https://doi.org/10.1039/c5py02009c.

Grellmann, W., & Seidler, S. (2015). *Kunststoffprüfung* (3rd ed.). München: Hanser

Guessasma, S., Tao, L., Belhabib, S., Zhu, J., Zhang, W., & Nouri, H. (2018). Analysis of microstructure and mechanical performance of polymeric cellular structures designed using stereolithography. *European Polymer Journal*, *98*, 72–82. https:// doi.org/10.1016/j.eurpolymj.2017.10.034.

Hague, R., Mansour, S., Saleh, N., & Harris, R. (2004). Materials analysis of stereolithography resins for use in rapid manufacturing. *Journal of Materials Science*, *39*(7), 2457–2464. https://doi.org/10.1023/B:JMSC.0000020010.73768.4a.

Homaeigohar, S., Shokrgozar, M. A., Khavandi, A., & Javadpour, J. H. (2005). *In vitro* evaluation of biocompatibility of beta-tricalcium phosphate-reinforced

high-density polyethylene; an orthopedic composite. *Journal of Biomedical Material Research A*, *75*, 14–22. https://doi.org/10.1002/jbm.a.30333.

Jan, S.-L., & Shieh, G. (2014). Sample size determinations for Welch's test in one-way heteroscedastic ANOVA. *British Journal of Mathematical & Statistical Psychology*, *67*(1), 72–93. https://doi.org/10.1111/bmsp.12006.

Kazmer, D., & Kutz, M. (2017). Three-dimensional printing of plastics, applied plastics engineering handbook-processing, materials, and applications. *Volume in Plastics Design & Library*, *2*, 617–634.

Kim, D. S. (D.)., Suriboot, J., Shih, C.-C., Cwiklik, A., Grunlan, M. A., & Tai, B. L. (2020). Mechanical isotropy and postcure shrinkage of polydimethylsiloxane printed with digital light processing. *Rapid Prototyping Journal*, *26*(8), 1447–1452. https://doi.org/10.1108/RPJ-10-2019-0255.

Kundu, A., Arnett, P., Bagde, A., Azim, N., Kouagou, E., Singh, M., & Rajaraman, S. (2020). DLP 3D printed "intelligent" microneedle array (iμNA) for stimuli responsive release of drugs and its *in vitro* and *ex vivo* characterization. *Journal of Microelectromechanical Systems*, *29*(5), 685–691. https://doi.org/10.1109/JMEMS.2020.3003628.

Lai, C. Q., Markandan, K., Luo, B., Lam, Y. C., Chung, W. C., & Chidambaram, A. (2021). Viscoelastic and high strain rate response of anisotropic graphene–polymer nanocomposites fabricated with stereolithographic 3D printing. *Additive Manufacturing*, *37*, 101721. https://doi.org/10.1016/j.addma.2020.101721.

Lantz, B. (2013). The impact of sample non-normality on ANOVA and alternative methods. *British Journal of Mathematical & Statistical Psychology*, *66*, 224–244. https://doi.org/10.1111/j.2044-8317.2012.02047.x.

Levy, K. J. (1978). Some empirical power results associated with Welch's robust analysis of variance technique. *Journal of Statistical Computation & Simulation*, *8*(1), 43–48. https://doi.org/10.1080/00949657808810246.

Li, H., Chen, J., Chandrashekhara, K., Xu, M., Lekakh, S. N., & Richards, V. L. (2015). Characterization and modeling of anisotropic SL pattern during investment casting process. *The International Journal of Advanced Manufacturing Technology*, *80*(9–12), 1933–1943. https://doi.org/10.1007/s00170-015-7090-6.

Li, Y., Peng, S., Miao, J.-T., Zheng, L., Zhong, J., Wu, L., & Weng, Z. (2020). Isotropic stereolithography resin toughened by core–shell particles. *Chemical Engineering Journal & the Biochemical Engineering Journal*, *394*, 124873. https://doi.org/10.1016/j.cej.2020.124873.

Ligon, S., Liska, R., Stampfl, J., Gurr, M., & Mülhaupt, R. (2017). Polymers for 3D printing and customized additive manufacturing. *Chemical Reviews*, *117*, 10212–10290. https://doi.org/10.1021/acs.chemrev.7b00074.

Ligon-Auer, S. C., Schwentenwein, M., Gorsche, C., Stampfl, J., & Liska, R. (2015). Toughening of photo-curable polymer networks: a review.

Low, I. M. (1998). Effects of load and time on the hardness of a viscoelastic polymer. *Materials Research Bulletin*, *33*(12), 1753–1758. https://doi.org/10.1016/S0025-5408(98)00179-2.

Low, I. M., & Shi, C. (1998). Vickers indentation responses of epoxy polymers. *Journal of Materials Science Letters*, *17*(14), 1181–1183. https://doi.org/10.1023/A:1006517005082.

Manière, C., Harnois, C., & Marinel, S. (2021). 3D printing of porcelain: Finite element simulation of anisotropic sintering. *The International Journal of Advanced Manufacturing Technology*, *116*(9–10), 3263–3275. https://doi.org/10.1007/s00170-021-07304-y.

Markandan, K., Seetoh, I. P., & Lai, C. Q. (2021). Mechanical anisotropy of graphene nanocomposites induced by graphene alignment during stereolithography 3D printing. *Journal of Materials Research*, *36*, 4262–4274. https://doi.org/10.1557/s43578-021-00400-5.

McLouth, T., Severino, J., Adams, P., Patel, D., & Zaldivar, R. (2017). The impact of print orientation and raster pattern on fracture toughness in additively manufactured ABS. *Additive Manufacturing*, *18*, 103–109. http://doi.org/10.1016/j.addma.2017.09.003.

Monzon, M., Ortega, Z., Hernandez, A., Paz, R., & Ortega, F. (2017). Anisotropy of photopolymer parts made by digital light processing. *Materials*, *10*(1), 64. https://doi.org/10.3390/ma10010064.

Ngo, T., Kashani, A., Imbalzano, G., Nguyen, K., & Hui, D. (2018). Additive manufacturing (3D printing): A review of materials, methods, applications and challenges. *Composites Part B: Engineering*, *143*, 172–196. https://doi.org/10.1016/j.compositesb.2018.02.012.

Quenard, O., Dorival, O., Guy, P., Votie, A., & Brethome, K. (2018). Measurement of fracture toughness of metallic materials produced by additive manufacturing. *CEAS Space Journal*, *10*(3), 343–353.

Randolph, L. D., Palin, W. M., Leloup, G., & Leprince, J. G. (2016). Filler characteristics of modern dental resincomposites and their influence on physico-mechanical properties. *Dental Materials*, *32*(12), 1586–1599. http://doi.org/10.1016/j.dental.2016.09.034.

Rath, T., Martl, O., Steyrer, B., Seidler, K., Addison, R., Holzhausen, E., & Stampfl, J. (2021). Developing an ivory-like material for stereolithography-based additive manufacturing. *Applied Materials Today*, *23*, 101016. https://doi.org/10.1016/j.apmt.2021.101016.

Razali, N. M., & Wah, Y. B. (2011). Power comparisons of Shapiro–Wilk, Kolmogorov–Smirnov, Lilliefors and Anderson–Darling tests. *Journal of Statistical Model Analytics*, *2*, 21–33.

Seitz, H., Deisinger, U., Leukers, B., Detsch, R., & Ziegler, G. (2009). Different calcium phosphate granules for 3-D printing ofbone tissue engineering scaffolds. *Advanced Engineering Materials*, *11*, 41–46. https://doi.org/10.1002/adem.200800334.

Shanmugasundaram, S., Razmi, J., Mian, J., & Ladani, L. (2020). Mechanical anisotropy and surface roughness in additively manufactured parts fabricated by stereolithography (SLA) using statistical analysis. *Materials*, *13*(11), 2496. https://doi.org/10.3390/ma13112496.

Sherry, A. H., & Marrow, T. J. (2010). *Shreir's corrosion* (vol. 1, 4th ed.). Amsterdam: Elsevier.

Vamze, J., Pilmane, M., & Skagers, A. (2015). Biocompatibility of pure and mixed hydroxyapatite and a-tricalcium phosphate implanted in rabbit bone. *Journal of Material Science: Materials in Medicine*, *26*, 73. https://doi.org/10.1007/s10856-015-5406-6.

Wang, R., Habib, E., & Zhu, X. X. (2018). Evaluation of the filler packing structures in dentalresin composites: From theory to practice. *Dental Materials*, *34*, 1014–1023. https://doi.org/10.1016/j.dental.2018.03.022.

Wang, X., Jiang, M., Zhou, Z., Gou, J., & Hui, D. (2017). 3D printing of polymer matrix composites: A review and prospective. *Composites Part B: Engineering*, *110*, 442–558. http://doi.org/10.1016/j.compositesb.2016.11.034.

Wang, Y., Zhou, Y., Lin, L., Corker, J., & Fan, M. (2020). Overview of 3D additive manufacturing (AM) and corresponding AM composites. *Composites Part A: Applied Science & Manufacturing*, *139*, 106114. https://doi.org/10.1016/j.compositesa.2020.106114.

Wille, S., Hölken, I., Galina, H., Adelung, R., & Kern, M. (2016). Biaxial flexural strength of new *Bis*-GMA/TEGDMA based composites with different fillers for dental applications. *Dental Materials*, *32*, 1073–1078. https://doi.org/10.1016/j.dental.2016.06.009.

Williams, D. (2008). On the mechanisms of biocompatibility. *Biomaterials*, *29*, 2941–2953. https://doi.org/10.1016/j.biomaterials.2008.04.023.

Wu, X., Xu, C., Zhang, Z., & Guo, C. (2020). Modeling and visualization of layered curing conversion profile in ceramic mask projection stereolithography process. *Ceramics International*, *46*(16), 25750–25757. https://doi.org/10.1016/j.ceramint.2020.07.053.

Zhao, C. Q., Xu, X. C., Lu, Y. J., Wu, S. Q., Xu, Z. Y., Huang, T. T., & Lin, J. X. (2020). Doping lithium element to enhance compressive strength of b-TCP scaffolds manufactured by 3D printing for bone tissue engineering. *Journal of Alloys & Compounds: Part A*, *814*, 152327. https://doi.org/10.1016/j.jallcom.2019.152327.

Zhiquan, L., Chong, W., Wanwan, Q., & Ren, L. (2019). Antimicrobial thiol-ene-acrylate photosensitive resins for DLP 3D printing. *Photochemistry & Photobiology*, *95*, 1219–1229. https://doi.org/10.1111/php.13099.

Zhou, T., Zhang, L., Yao, Q., Ma, Y., Hou, C., Sun, B., … Chen, H. (2020). SLA 3D printing of high quality spine shaped β-TCP bioceramics for the hardtissue repair applications. *Ceramics International*, *46*(6), 7609–7614. https://doi.org/10.1016/j.ceramint.2019.11.261.